



Dual-stage repetitive control with Prandtl–Ishlinskii hysteresis inversion for piezo-based nanopositioning

Yingfeng Shan, Kam K. Leang*

Department of Mechanical Engineering, University of Nevada – Reno, Reno, NV 89557-0312, USA

ARTICLE INFO

Article history:

Available online 24 December 2011

Keywords:

Repetitive control
Hysteresis
Nanopositioning
Prandtl–Ishlinskii hysteresis modeling

ABSTRACT

The positioning performance of piezo-based nanopositioning systems is limited by dynamic and hysteresis effects in the piezoactuator. Herein, a high-performance, dual-stage repetitive controller (dual-RC) with a feedforward hysteresis compensator is proposed for tracking periodic trajectories, such as the scanning-type motion, in nanopositioning systems. Firstly, a discrete-time dual-RC is created by cascading a conventional RC with an odd-harmonic RC. The favorable gain characteristics of the dual-RC coincide with the odd harmonics of the scanning-type periodic reference trajectory, thus offering good robustness and low tracking error. Secondly, a new inverse-hysteresis compensator is developed based on the Prandtl–Ishlinskii hysteresis model. The structure of the inverse model mimics the structure of the forward model, where the parameters of the inverse model can be easily identified from measured input–output data. Finally, the controllers are applied to a custom-designed high-speed nanopositioner, and simulations and experimental results are provided to illustrate the performance improvement of the proposed control scheme compared to industry-standard PID control and conventional RC. High-speed positioning results (tracking of triangle scan trajectories) at rates of 1 kHz, 1.5 kHz, and 2 kHz are shown. Compared to a conventional RC, the tracking error of the dual-RC is 48% lower at 1 kHz and 33% lower at 2 kHz scanning frequency. It is also shown that by compensating for hysteresis, the performance of the RC system designed based on the linear dynamics can be enhanced.

© 2011 Elsevier Ltd. All rights reserved.

1. Introduction

Multi-axis piezo-based nanopositioners are critical tools for emerging and enabling nanotechnology applications, such as scanning probe microscopes (SPMs). Often times, these nanopositioners are required to track periodic reference trajectories with precision. For example, in an atomic force microscope (AFM), a type of SPM, a nanopositioner is used to precisely position a tool tip relative to a sample surface to obtain high-resolution topographical images, directly measure various properties of a specimen, and even investigate nano-scale dynamic interactions in real time [1–3]. However, the response of the piezoactuator exhibits hysteresis and dynamic effects, the latter being creep and vibration, which make controlling the piezoactuator's movements a challenge. Precision control of the piezoactuator is needed to hold the SPM-probe tip at a desired location or to track a desired motion trajectory, such as the scanning trajectory in AFM imaging or nanofabrication. In SPM-probe-based nanofabrication, precise position control of the indenter tip is needed because the probe position error directly affects the size, spacing,

and distribution of the nanofeatures. Even variations in the probe position of a few nanometers can drastically affect the resulting size and spacing of the nanofeatures created with the probe tip. Moreover, high-speed control of the probe's movement is needed for high throughput fabrication, imaging, and metrology. Without precise motion control at high-speed, oscillations can cause the tip to collide with nearby features, which leads to excessive tip-to-sample forces. The large forces can damage, for example, the probe or soft specimens such as live cells. The main contribution of this paper is the development of a dual-stage repetitive controller combined with a new inverse-hysteresis compensator to track periodic trajectories in piezo-based nanopositioning systems. The control approach is well suited for scanning-type applications where the desired motion is periodic in time and dominated by odd harmonics.

Repetitive control is a direct application of the internal model principle [4], where a signal generator is incorporated into a feedback loop to provide high gain at the fundamental frequency of the reference trajectory and its harmonics [5,6]. Recently, the RC approach was studied for scanning applications in piezo-based AFMs [7]. Repetitive controllers have also been used to address run-out issues in disk drive systems [8,9] and to improve the performance of machine tools [10,11]. Compared to traditional proportional-integral or proportional-integral-derivative (PID)

* Corresponding author. Tel.: +1 775 784 7782; fax: +1 775 784 1701.

E-mail address: kam@unr.edu (K.K. Leang).

feedback controllers, where careful tuning is required and the residual tracking error persists from one operating cycle to the next, RC has the ability to reduce the error as the number of operating cycles increases. For applications in which the desired trajectory is periodic and the signal period is known *a priori*, a repetitive controller offers many advantages. Firstly, it can be plugged into an existing feedback control loop to enhance performance for scanning applications. Secondly, compared to iterative learning control (ILC) [12,13], a control method that has been used extensively for piezo-based positioning systems [14,15], RC does not require the initial condition to be reset at the start of each iteration trial [6]. Therefore, the implementation is simplified. Thirdly, compared to model-based feedforward approaches [16,17], RC does not require extensive modeling of the system. Due to variations in the system dynamics, for example those caused by aging [18] or temperature variations [19], open-loop feedforward approaches often lack robustness. On the other hand, the feedback mechanism built into RC provides robustness to parameter variation. Finally, RC can be easily implemented digitally, and thus high-speed data acquisition and control hardware such as field-programmable gate array systems [20] can take advantage of the RC structure for precision control.

The challenges with designing and implementing RC include stability, robustness, and achieving good steady-state tracking performance. One solution to the stability and robustness problem is to incorporate a low-pass filter into the RC loop [21] or employ a simple frequency aliasing filter [22]. It is pointed out that a tradeoff is made between robustness and high frequency tracking when such filters are used. The steady-state tracking performance of RC can be improved, for example, by cascading a phase-lead compensator to account for the phase lag of the low-pass filter to increase the controller gain at the harmonics of the reference trajectory [23,7]. High-order RC has been studied in [9] to improve performance and robustness in the presence of noise and variations in the signal period.

The work on the design of RC for systems which exhibit dynamic and hysteresis effects is limited. Herein, a high-performance, dual-stage repetitive controller (dual-RC) with a feedforward hysteresis compensator is proposed for systems like piezo-based nanopositioners. Firstly, the design of the dual-RC is motivated by the need to further reduce the magnitude of the sensitivity function of the closed-loop system to help lower the tracking error. This is achieved by cascading a conventional RC with an odd-harmonic RC [24,25], effectively ‘squaring’ the controller. This structure not only lowers the tracking error compared to conventional RC, but also offers good robustness for tracking odd-harmonic trajectories. It is noted that a similar dual-RC structure has been studied in [26], where two identical RCs are cascaded together (series connection); and a parallel configuration is presented in [24,25]. In contrast, the proposed dual-RC cascades an enhanced conventional RC with an odd-harmonic RC, and the series configuration is specifically tailored for tracking periodic scanning trajectories such as triangle signals with odd harmonics. Such reference signals are commonly used in piezo-based nanopositioners for raster-type and scanning applications, like AFM imaging. To assist a designer in choosing the controller parameters for optimum performance, the stability analysis for the dual-RC is presented.

Secondly, the hysteresis behavior in the piezoactuator is accounted for using a new inverse-hysteresis feedforward controller. Hysteresis compensation is critical because the effect, if left unaccounted for, can affect the system stability [27,28]. The hysteresis compensator is based on the Prandtl–Ishlinskii model, a phenomenological model for hysteresis where the output is a superposition of weighted play or stop operators [29–31]. To create the inverse model, a new play-type operator is proposed which is motivated by the shape of the hysteresis curve. The new operator enables

the development of an inverse model that takes the same form as the forward P-I model, and importantly, the parameters of the inverse model are determined from the measured hysteresis curve using the same technique as the forward model. Compared to other models for hysteresis such as polynomial models [32], the Bouc–Wen model [33,34], the Duhem model [35,36], the Maxwell slip model [37], and the Preisach model [38–41], the P-I model can accurately model symmetric hysteresis loops with a smaller set of parameter, and thus the model inversion is more efficient and less computationally demanding for real-time feedforward control. It is pointed out that charge control [42,46] can be used in place of the hysteresis compensator, but this approach requires a specialized charge-control circuit. The main contribution of this paper is the design and analysis of a new dual-RC combined with a new hysteresis feedforward compensator to improve the performance of piezo-based nanopositioning systems for scanning-type applications. Simulation and experimental results are presented to demonstrate the effectiveness of the control approach.

The remainder of the paper is organized as follows. Section 2 presents the dual-RC design and stability analysis. Section 3 discusses the hysteresis modeling and the inverse hysteresis compensator design. Section 4 describes the experimental system and the dynamics and hysteresis modeling. Section 5 describes the controller design, simulation, and experimental results. Finally, Section 6 concludes the paper.

2. Design of repetitive control for periodic trajectory tracking

Repetitive control is a feedback-based approach suited for tracking periodic trajectories and/or for rejecting periodic disturbances. To do this, an RC provides large gain at the harmonics of the reference trajectory by incorporating a signal generator within the feedback loop [7–9]. For piezo-based nanopositioning systems, the RC must be designed for low tracking error in the presence of dynamic and hysteresis effects. To aid in designing the RC, the dynamic and hysteresis effects in a piezoactuator is described by a cascade model (see system block in Fig. 1a) [43]. The hysteresis behavior is captured by a rate-independent input nonlinearity $\mathcal{H}[\cdot]$ and the output of this nonlinearity becomes the input that drives a linear dynamics model $G(s)$ which

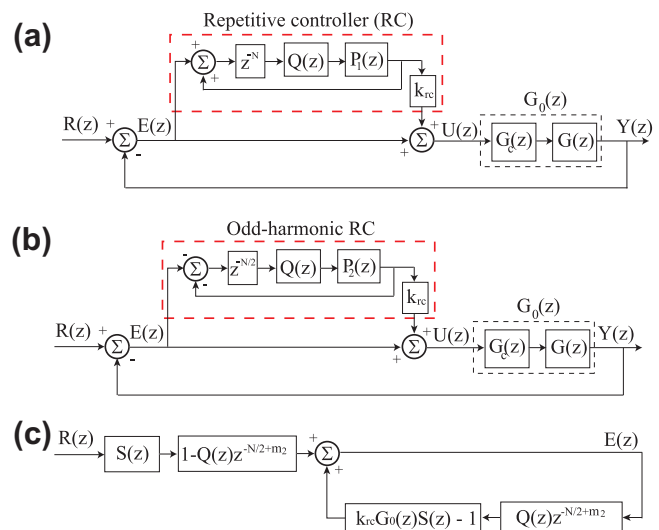


Fig. 1. (a) A conventional RC system, where the $R(z)$ represents a periodic reference trajectory, $Y(z)$ is the system output, $G_c(z)$ is the controller and $G(z)$ is the plant dynamics. (b) An odd-harmonic RC with a linear phase-lead compensator $P_2(z) = z^{m_2}$ and a RC gain k_{rc} to enhance performance. (c) An equivalent block diagram of (b) for stability analysis.

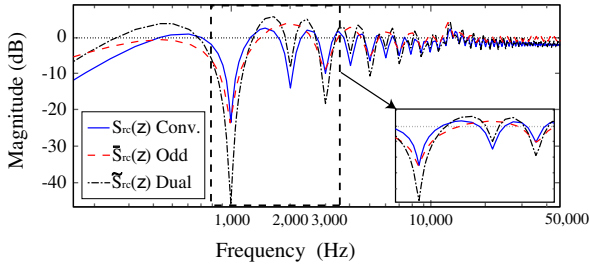


Fig. 3. Comparison of magnitude versus frequency plots for the sensitivity functions for different RC configurations, where $S_{rc}(z)$ denotes the conventional RC (solid line), $\tilde{S}_{rc}(z)$ is for the odd-harmonic RC (dash line), and $\tilde{\tilde{S}}_{rc}(z)$ represents the dual-RC (dash-dot line).

of trajectories with odd-harmonics. The stability analysis of the odd-harmonic RC and the enhanced dual-RC is discussed in the following.

2.3. Stability analysis

The stability of the RC system is analyzed using the Small Gain Theorem [45].

2.3.1. Stability analysis of the odd-harmonic RC

Let T_s be the sampling time. Consider the odd-harmonic RC shown in Fig. 1b and the following assumptions:

Assumption 1. The reference trajectory $R(z)$ is periodic in time with period T_p .

Assumption 2. The closed-loop system without the RC is asymptotically stable, i.e., $1 + G_0(z) = 0$ has no roots outside of the unit circle in the z -plane.

The main result for the stability conditions for the odd-harmonic RC is provided in the following theorem:

Theorem 1 (Stability of odd-harmonic RC). Let Assumptions 1 and 2 hold. If $|Q(e^{j\omega T_s})| \leq 1$ and

$$0 < k_{rc} < \frac{2 \cos[\theta_T(\omega)]}{A(\omega)} \quad \text{and} \quad -\pi/2 < \theta_T(\omega) < \pi/2, \quad (6)$$

for $\omega \in (0, \pi/T_s)$, then the RC feedback system shown in Fig. 1b is asymptotically stable.

Proof. First, the RC block diagram in Fig. 1b is simplified to the equivalent interconnected system shown in Fig. 1c. Since $1 - H_2(z)$ and $S(z)$ are stable, then the RC system in Fig. 1b is asymptotically stable when

$$\left| z^{-\frac{N}{2} + m_2} Q(z) [k_{rc} G_0(z) S(z) - 1] \right| < 1. \quad (7)$$

Noting that $z = e^{j\omega T_s}$, $|Q(e^{j\omega T_s})| \leq 1$, and the complimentary sensitivity function of the closed-loop system without the RC is given by Eq. (1), condition (7) is satisfied if

$$|k_{rc} A(\omega) e^{j\theta_T(\omega)} - 1| < 1. \quad (8)$$

Letting $e^{j\theta} = \cos(\theta) + j\sin(\theta)$ and $k_{rc} > 0$, Eq. (8) gives

$$-2k_{rc} A(\omega) \cos[\theta_T(\omega)] + k_{rc}^2 A^2(\omega) < 0, \quad (9)$$

hence

$$0 < k_{rc} < \frac{2 \cos[\theta_T(\omega)]}{A(\omega)} \quad \text{and} \quad -\pi/2 < \theta_T(\omega) < \pi/2.$$

This completes the proof. \square

The results of Theorem 1 states that within an acceptable operating frequency range, there exists a sufficiently small RC gain k_{rc} such that the closed-loop RC system is stable. Next, the stability conditions for the dual-RC, created by cascading an odd-harmonic RC with the conventional RC, is presented.

2.3.2. Stability analysis of the enhanced dual-RC

Consider the enhanced dual-RC system shown in Fig. 2a and Assumptions 1 and 2 from above. The stability conditions are summarized in the following theorem.

Theorem 2 (Stability of enhanced dual-RC). Let Assumptions 1 and 2 hold. If $|Q(e^{j\omega T_s})| \leq 1$ and

$$\begin{aligned} \frac{3 \cos[\theta_T(\omega)] - \Delta}{3A(\omega)} &< k_1, k_2 \\ &< 1 + \sqrt{1 + \frac{3 \cos[\theta_T(\omega)] + \Delta}{3A(\omega)}}, \\ &-\pi/9 \leq \theta_T(\omega) \leq \pi/9, \end{aligned} \quad (10)$$

with $\Delta = \sqrt{9 \cos^2[\theta_T(\omega)] - 8}$ for $\omega \in (0, \pi/T_s)$, then the closed-loop system in Fig. 2a is asymptotically stable.

Proof. First, recall that if $a, b, c, d \in \mathbb{C}$, where \mathbb{C} is the set of all complex numbers, and $|a| \leq 1$, $|c| \leq 1$ and $|b| + |d| \leq 1$, then $|a||b| + |c||d| \leq 1$. Now the sensitivity function in Eq. (4) is modified to

$$\tilde{\tilde{S}}_{rc}(z) = \frac{[1 - H_1(z)][1 - H_2(z)]S(z)}{1 - [H_1(z)\lambda_1(z) + H_2(z)\lambda_2(z) - H_1(z)H_2(z)\lambda_3(z)]S(z)}, \quad (11)$$

where $\lambda_1(z) = 1 + (1 - k_1)G_0(z)$, $\lambda_2(z) = 1 + (1 - k_2)G_0(z)$, and $\lambda_3(z) = 1 + (1 - k_1)(1 - k_2)G_0(z)$. The RC system in Fig. 2a is converted to the equivalent interconnected system shown in Fig. 2b.

Then, according to Fig. 2b and the Small Gain Theorem, the dual-RC system is internally stable when

$$|[H_1(z)\lambda_1(z) + H_2(z)\lambda_2(z) - H_1(z)H_2(z)\lambda_3(z)]S(z)| < 1, \quad (12)$$

with $1 - H_1(z)$ and $1 - H_2(z)$ designed stable. Applying the triangle inequality and noting that $|H_1(z)| \leq 1$ and $|H_2(z)| \leq 1$,

$$\begin{aligned} |[H_1(z)\lambda_1(z) + H_2(z)\lambda_2(z) - H_1(z)H_2(z)\lambda_3(z)]S(z)| \\ \leq |\lambda_1(z)S(z)| + |\lambda_2(z)S(z)| + |\lambda_3(z)S(z)|. \end{aligned} \quad (13)$$

Then Eq. (12) is satisfied if

$$|\lambda_1(z)S(z)| + |\lambda_2(z)S(z)| + |\lambda_3(z)S(z)| < 1. \quad (14)$$

Noting that $T(z) = G_0(z)S(z)$ and replacing $z = e^{j\omega T_s}$, the gains k_i with $i = 1, 2$ can be determined from Eq. (14) as follows:

First, if $|\lambda_3(z)| \leq |\lambda_i(z)|$ Eq. (14) can be simplified to

$$|\lambda_1(z)S(z)| + |\lambda_2(z)S(z)| + |\lambda_i(z)S(z)| < \begin{cases} 3|\lambda_1(z)S(z)| < 1, & \forall k_1 \leq k_2 \\ 3|\lambda_2(z)S(z)| < 1, & \forall k_2 \leq k_1 \end{cases}$$

thus

$$3|1 - k_i T(e^{j\omega T_s})| < 1, \quad k_i = \max(k_1, k_2). \quad (15)$$

Second, if $|\lambda_3(z)| \geq |\lambda_i(z)|$, then

$$3|1 - (2k_i - k_i^2)T(e^{j\omega T_s})| < 1. \quad (16)$$

Third, if $|\lambda_j(z)| \leq |\lambda_3(z)| \leq |\lambda_i(z)|$, $j \neq i$, $j \in \{1, 2\}$, $i \in \{1, 2\}$, Eq. (14) can also be simplified to

$$|\lambda_1(z)S(z)| + |\lambda_2(z)S(z)| + |\lambda_i(z)S(z)| < \begin{cases} 3|\lambda_1(z)S(z)| < 1, & \forall k_1 \leq k_2 \\ 3|\lambda_2(z)S(z)| < 1, & \forall k_2 \leq k_1 \end{cases}$$

thus

$$3 | 1 - k_i T(e^{j\omega T_s}) | < 1, \quad k_i = \max(k_1, k_2). \quad (17)$$

Therefore, the gains are found by solving Eqs. (15)–(17), i.e.,

$$\frac{3 \cos[\theta_T(\omega)] - \Delta}{3A(\omega)} < k_1, k_2 < 1 + \sqrt{1 + \frac{3 \cos[\theta_T(\omega)] + \Delta}{3A(\omega)}},$$

$$-\pi/9, \leq \theta_T(\omega) \leq \pi/9,$$

with $\Delta = \sqrt{9 \cos^2[\theta_T(\omega)] - 8}$. This completes the proof. \square

By satisfying the conditions in **Theorem 2**, that is, by picking appropriate values for the RC gains, k_1 and k_2 , within a particular operating frequency range, the dual-RC is guaranteed stable. Next, a new inverse-hysteresis compensator is proposed to handle the hysteresis effect.

3. Hysteresis compensation: the Prandtl–Ishlinskii (P-I) hysteresis model

The proposed dual-RC design assumes that the piezoactuator dynamics are linear; however, it is a well-known fact that hysteresis behavior is significant in piezo-based nanopositioning systems [17,16]. It has been noted that the nonlinearity can affect closed-loop stability if not accounted for [27,28]. Rather than deal with the hysteresis effect directly by designing a nonlinear RC, a task that is complex, instead a feedforward hysteresis compensator is proposed to minimize the effect. This way, the RC controller can be redesigned as needed using linear control techniques and thus be decoupled from the design of the hysteresis compensator. As pointed out, for piezo-based nanopositioning systems, the dynamic and hysteresis effects in a piezoactuator is described by a cascade model [43]. The range-dependent hysteresis effect of the piezoactuator is treated as a rate-independent input nonlinearity $\mathcal{H}[\cdot]$ and an inverse-hysteresis controller is proposed based on the Prandtl–Ishlinskii (P-I) hysteresis model and a new play-type hysteresis operator. Some of the advantages of the P-I model compared to other hysteresis models (such as the Preisach model) is smaller number of parameters for more efficient on-line implementation. The control structure is shown in Fig. 4, where the feedforward compensator appears before the piezoactuator system to compensate for hysteresis.

3.1. The Prandtl–Ishlinskii hysteresis model

The Prandtl–Ishlinskii model is an operator-type, phenomenological model for rate independent hysteresis behavior; it has recently been investigated to model hysteresis in piezoactuators [29–31]. The model’s output $u(t)$ is a weighted superposition of elementary hysteresis operators, play or stop operators [29], as shown in Fig. 5a. Let the input $u(t) \in C_m[t_a, t_b]$, where $C_m[t_a, t_b]$ represents the space of piecewise monotone continuous functions defined over time period $\{t : t_a \leq t \leq t_b; 0 \leq a \leq b \in \mathbb{N}\}$. Specifically, the play operator is defined as

$$\mathcal{P}_r[u](0) = p_r(f(0), 0) = 0,$$

$$\mathcal{P}_r[u](t) = p_r(f(t), \mathcal{P}_r[f](t)), \quad (18)$$

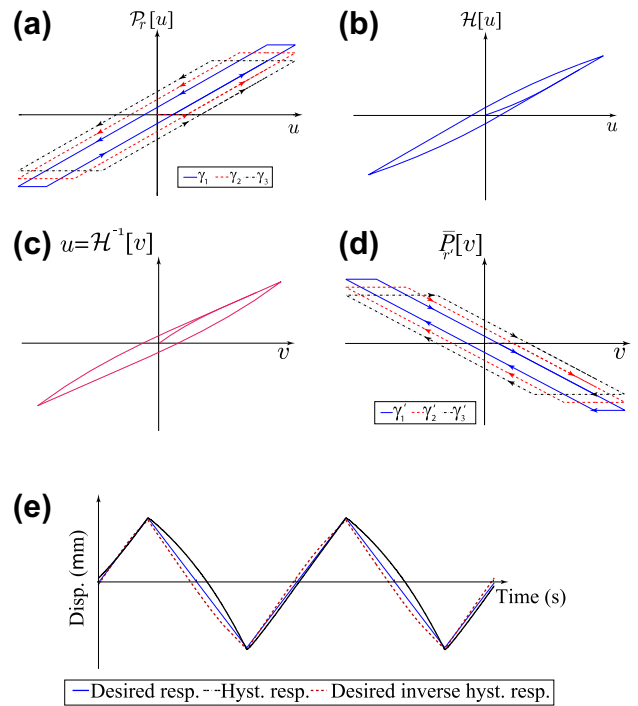


Fig. 5. P-I hysteresis model: (a) The play operator with threshold γ_i . (b) An example output versus input plot for the Prandtl–Ishlinskii hysteresis model for a piezoactuator. (c) Inverse hysteresis curve: input versus output plot. (d) A play-type operator for the inverse model with threshold γ'_i . (e) Time response comparing the desired response (solid line), hysteresis response (dash-dot line), and inverse hysteresis output (dash line).

where $p_r(f(t_i), \mathcal{P}_r[f](t_i)) = \max(f(t_i) - \gamma, \min(f(t_i) + \gamma, \mathcal{P}_r[f](t_{i-1})))$, $f(t) = g_0 u(t) + g_1$ with constants g_0 and g_1 , and γ is the input threshold [29]. The output $u(t)$ of the P-I model is defined as

$$v(t) = \mathcal{H}[u](t) \triangleq f(t) + \int_0^R d(\gamma) \mathcal{P}_r[u](t) d\gamma, \quad (19)$$

where $d(\gamma)$ is the density function that controls the shape and size of the hysteresis curve. Fig. 5a shows an example of play operators with threshold γ_i , for $i = 1, 2, 3$, and Fig. 5b is an example output versus input (hysteresis) plot for the P-I model. The parameters of the P-I model can be determined experimentally and this process is described below in Section 4.3.

3.2. An inverse hysteresis feedforward compensator

To compensate for the hysteresis behavior, an inverse P-I model is proposed. The characteristics of the inverse model is based on the characteristic shape of the inverse hysteresis curve, that is, the input versus output curve shown in Fig. 5c (u versus v plot). It is noted that as the output v increases, the input u increases but traverses onto an upper branch of the inverse-hysteresis curve. In contrast, this behavior is opposite to that observed in

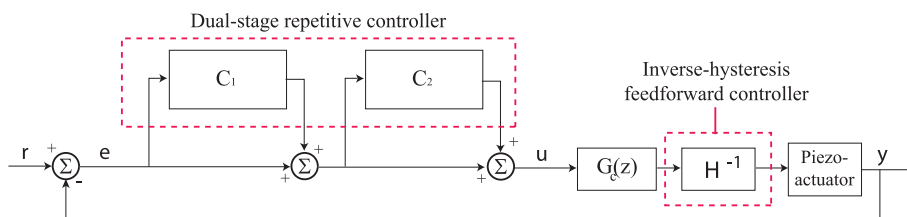


Fig. 4. The dual-RC closed loop system with feedforward hysteresis compensator.

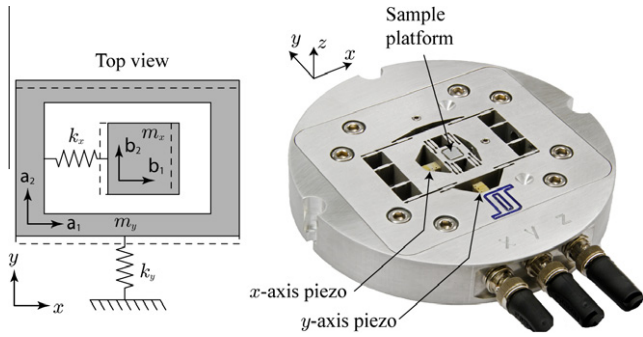


Fig. 6. The serial-kinematic three-axis nanopositioning system.

the hysteresis curve (v versus u plot) where the output climbs up on a lower branch as shown in Fig. 5b. Therefore, a candidate play-type operator for the inverse-hysteresis model is shown in Fig. 5d. Fig. 5e compares the time responses between the desired output (solid line), output from a hysteretic system (dash-dot line), and the output from the proposed inverse-hysteresis model (dash line). Using this operator offers the advantage that the structure of the forward model can be used directly to map the desired output to the hysteresis-compensating feedforward input. In other words, the P-I output Eq. (19) becomes the inverse map simply by setting the output equal to the input and vice versa. It is noted that the input–output response for the inverse model shown in Fig. 5c is a reflection of Fig. 5b about the axis $u = v$. Therefore, the inverse operator shown in Fig. 5d is defined as

$$\begin{aligned} \bar{P}_r[v](0) &= \bar{p}_r(h(0), 0) = 0, \\ \bar{P}_r[v](t) &= \bar{p}_r(h(t), \bar{P}_r[h](t)), \end{aligned} \quad (20)$$

where $\bar{p}_r(h(t_i), \bar{P}_r[h](t_i)) = \max(-h(t_i) - \gamma', \min(-h(t_i) + \gamma', \bar{P}_r[h](t_{i-1})))$, $h(t) = g'_0 v(t) + g'_1$ with constants g'_0 and g'_1 , and $u(t)$ is the output of the hysteresis behavior. The term γ' denotes the threshold of the proposed inverse play operator. Using this proposed inverse play-type operator, the output of the inverse-hysteresis model is given by

$$\mathcal{H}^{-1}[v](t) \triangleq h(t) + \int_0^R d_{inv}(\gamma') \bar{P}_r[v](t) d\gamma', \quad (21)$$

where $d_{inv}(\gamma')$ is the density function of the inverse P-I model. The performance of the inverse P-I hysteresis compensator is validated in simulations and experiments on a custom-designed high-speed nanopositioning stage described below.

4. The experimental nanopositioning system and modeling

The control approach is evaluated on a new custom-made, three-axis, flexure-guided serial-kinematic nanopositioning system. The experimental system is shown in Fig. 6 and the design of a similar stage is described in [49] for the interested reader.

The serial-kinematic configuration is specifically created for scanning-type applications. For scanning-type applications, such as the rastering movements in AFM imaging, one lateral axis moves much faster (>100 -times) than the other axis. Because of this, one axis is designed to have a significantly higher mechanical resonance [3,47]. Compliant double-hinged flexures are used to guide the lateral stages in their corresponding actuation directions while limiting out-of-plane (parasitic) motion and dynamic cross coupling. The high-speed (HS) x -stage and the low-speed (LS) y -stage use stiff plate-stack piezoactuators ($5 \times 5 \times 10$ mm Noliac SCMAP07) configured serially to provide lateral displacement. Not shown are the details of the z -stage, in which a piezo-stack is embedded into the x -stage body and the free ends secured with plate flexures, where a similar design is described in [48]. The stage is outfitted with inductive sensors (Kaman SMU9000-15N) to measure the displacement in the lateral directions. The lateral (x/y) range of motion is determined to be approximately $10 \times 10 \mu\text{m}$.

The first mechanical resonance for the high-speed x - and low-speed y -stage is 11.10 kHz and 4.68 kHz, respectively. The measured frequency responses of the stage are shown in Fig. 7. The results show that the dominant resonances are second-order in nature, and they are actuation modes.

4.1. Control hardware

The experimental system consists of a field-programmable gate array (FPGA) real-time controller with data acquisition modules, the nanopositioner, piezo amplifier, and inductive displacement sensors as shown in Fig. 8. Also, a desktop computer with a data acquisition card (NI-PCI-6221, 16-bit, maximum sampling frequency 250 kHz) is used to send reference signals to the FPGA controller and for collecting displacement data.

The FPGA system (National Instruments cRIO-9002) is used to implement the RC and PID controllers. The FPGA is programmed using the NI LabVIEW FPGA Toolkit to generate executable VHDL code that is downloaded to the target FPGA module for execution. The coding and downloading process is illustrated in Fig. 8. The FPGA system includes a real-time controller and 16-bit plug-in modules for AI (Analog Input) and AO (Analog Output). The maximum sampling frequency for the FPGA's data acquisition modules is 100 kHz.

4.2. Linear dynamics modeling

As an illustrative example, the control method is applied to the fast-scanning direction, x , of the nanopositioner. The linear dynamics model $G(s)$ for the x -axis is determined using a black-box identification technique. First, the frequency response of the piezoactuator is measured using a dynamic signal analyzer. The response is measured by driving the piezoactuator over a small displacement range ($<1 \mu\text{m}$) to minimize hysteresis effect and above 100 Hz to avoid creep in the piezoactuator. Then, the response is

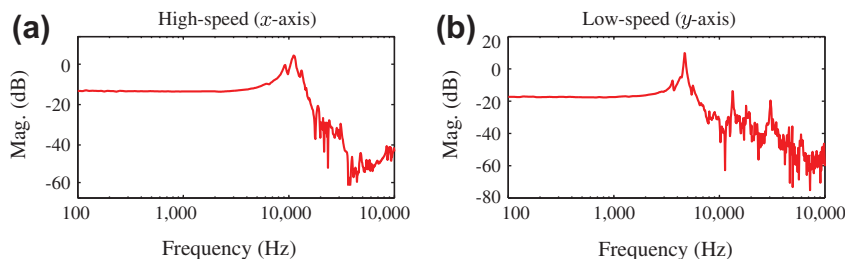


Fig. 7. Measured frequency response of nanopositioning stage: (a) high-speed axis and (b) low-speed axis.

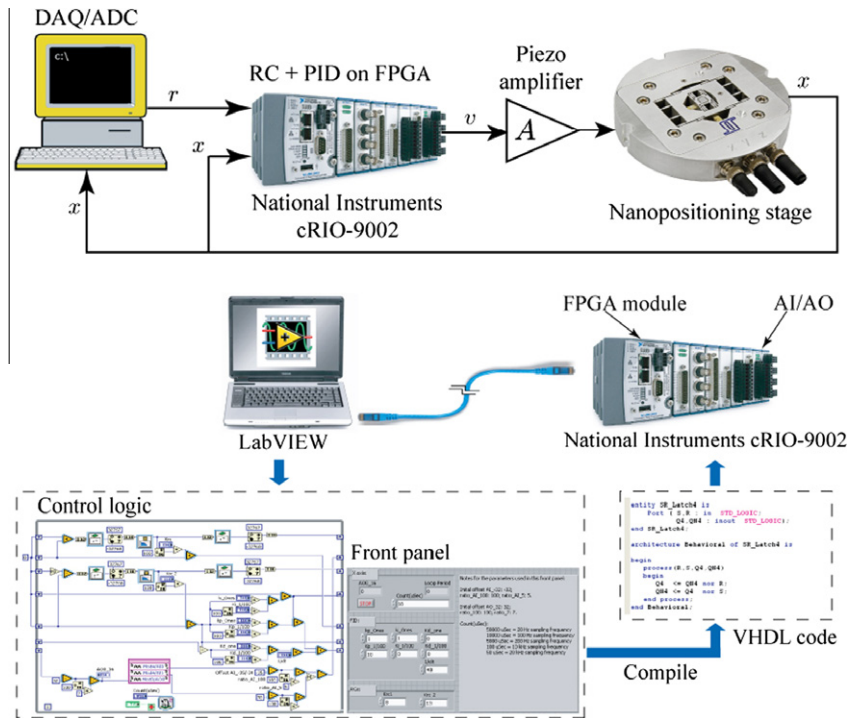


Fig. 8. The experimental system and the FPGA coding process: the VHDL code is generated using LabVIEW FPGA Toolkit, then downloaded to the real-time controller through an ethernet cable.

curve-fitted in Matlab to a linear model, a 9th-order transfer function model $G(s)$. Finally, the continuous-time model is converted to a discrete-time model $G(z)$ using the 'c2d' command in Matlab with a sampling frequency of 100 kHz. The model and measured response are in good agreement up to a frequency of 25 kHz, well above the dominant resonance.

4.3. Hysteresis modeling

The P-I model is used to characterize the hysteresis behavior in the piezoactuator along the x -axis. First, the hysteresis response is measured by actuating the piezoactuator with a triangle input signal at 10 Hz, full range. The 10 Hz frequency is chosen to avoid the creep effect and minimize the dynamics. Then the input voltage $u(t)$ and the response $x(t)$ are collected and imported to Matlab to a custom-designed least-square optimization program to calculate the P-I parameters. The parameters include g_0 and g_1 for $f(t) = g_0u(t) + g_1$; and λ , δ and ρ for density function $d(\gamma) = \lambda e^{-\delta\gamma}$, where $\gamma = \rho j$ for $j = 1, 2, \dots, n$. The parameters of the P-I model were identified as: $g_0 = 0.6081$, $g_1 = 0.0039$, $\lambda = 4.7649$, $\delta = 3.434$ and $\rho = 0.0769$ with eight play operators $j = 8$. Finally, the hysteresis model is validated by comparing the model's response with the measured response as presented in Fig. 9. The maximum modeling error is less than 1.87% and the root-mean-square of the error is 1.39%.

The hysteresis and dynamics model for the piezoactuator is created by cascading the P-I model $\mathcal{H}[\cdot]$ with the linear dynamics model $G(s)$. The open-loop response of the model is compared to the measured open-loop response of the piezoactuator. The responses are generated by applying a triangle input signal (100 Hz and 1 kHz) to the model and the experimental system such that the displacement is $\pm 5 \mu\text{m}$. The results are shown in Fig. 10 for the 100 Hz and 1 kHz responses. It is noted that the maximum error between the model and measured response is less than 2% up to a scanning frequency of 1 kHz. Therefore, the cascade model structure based on the P-I model is relatively accurate for modeling the combined hysteresis and dynamic effects in the piezoactuator.

5. Controller designs and tracking results

5.1. Dual-RC controller design and implementation

The design and implementation of the dual-RC begins with the design of the PID controller. The PID controller transfer function is given by $G_c(z) = K_p + K_i \frac{z}{z-1} + K_d \frac{z-1}{z}$, and the controller gains are tuned experimentally, with the initial values obtained using the Ziegler-Nichols method. The gains are $K_p = 1.1$, $K_i = 0.5$, and $K_d = 4$ with a sampling frequency of 100 kHz.

The two RC controllers, C_1 and C_2 (see Fig. 2b), are designed independently. First, C_1 is designed using the following steps: (1) design the low-pass filter $Q(z)$ for stability, (2) pick the RC gain, k_1 , to satisfy the stability condition in Theorem 2, and (3) design the phase lead compensator $P_1(z)$ to minimize the steady-state tracking error. Then the same process is applied to design C_2 . A systematic approach to design the RC gain and phase lead values are describe in [7]. Afterwards, C_1 and C_2 are cascaded together to create the dual-RC system, and subsequently the RC gains k_1 and k_2 are further adjusted for optimum tracking performance.

Step 1. The low-pass filters $Q(z)$ in both RC's are chosen as a first-order filter for convenience, i.e., $Q(z) = a/(z + b)$ with $|a| + |b| = 1$. The cutoff frequency is selected based on the stability

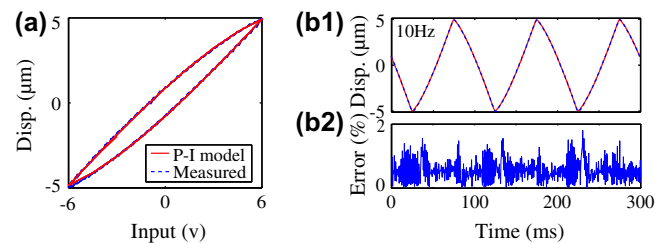


Fig. 9. Comparison of measured hysteresis behavior to the output of the P-I hysteresis model at 10 Hz. (a) The hysteresis curves. (b1) and (b2) The displacement and the error between measured and model output versus time at 10 Hz.

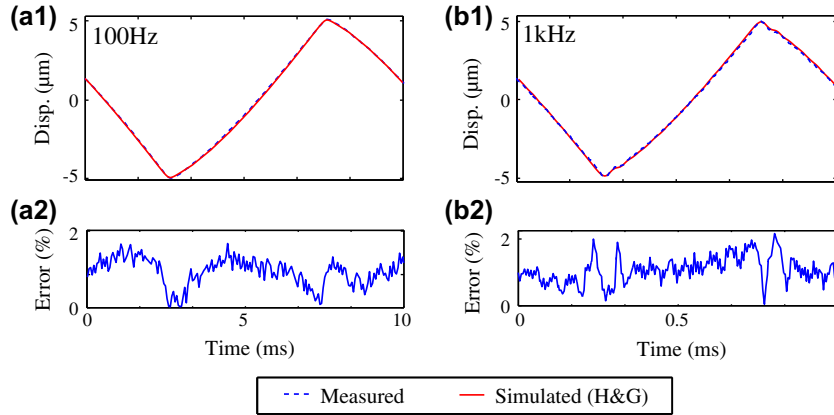


Fig. 10. Experimental validation of the system model, $\mathcal{H}[\cdot]$ cascaded with $G(z)$, of the piezoactuator. The displacement and error between the measured and model output versus time at (a1) and (a2) 100 Hz and (b1) and (b2) 1 kHz scanning.

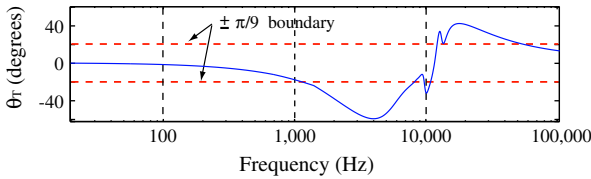


Fig. 11. The phase response of the PID closed-loop feedback system without the RCs.

condition given in Eq. (10) to ensure that the phase of the closed-loop system without the RCs falls between $-\pi/9 \leq \theta_T(\omega) \leq \pi/9$, for $\omega \in (0, \pi/T_s)$. Using the linear dynamics model $G(z)$ and the PID controller $G_c(z)$, the frequency where $\theta_T(\omega)$ becomes larger than $\pm\pi/9$ is approximately 1.3 kHz as shown in Fig. 11. However, it is pointed out that the condition given in Eq. (10) may be conservative, and thus simulations are performed to determine a more practical cutoff frequency for high-speed positioning. Through simulation, the maximum cutoff frequency is found to be 7.5 kHz, and above that the RC system becomes unstable. Therefore the cutoff frequency of the low-pass filter is selected as 7 kHz.

Steps 2 and 3. The RC gain k_1 and phase lead compensator $P_1(z) = z^{m_1}$ are determined by simulating the RC control system for tracking a 1.5 kHz triangle reference trajectory. Firstly, the maximum tracking error is defined as

$$e_{max}(\%) = \left[\frac{\max |y(t) - r(t)|}{\max(r(t)) - \min(r(t))} \right] \times 100\%$$

where r and y are the reference and measured output, respectively. The RC gain is selected as $k_1 = 0.8$ by observing the smallest maximum tracking error in simulation. The value for m_1 is then determined using the same method with $k_1 = 0.8$. The maximum steady-state tracking error for different values of m_1 is presented in Fig. 12a. The optimum value for m_1 to provide the lowest steady-state tracking error is determined to be $m_1 = 6$. Likewise, for C_2 , the values are $k_2 = 1.2$ and $m_2 = 6$.

The controllers C_1 and C_2 are combined to create the dual-RC system as depicted in Fig. 2. Finally, the RC gains are further tuned in simulation to $k_1 = 0.8$ and $k_2 = 1.1$ for optimum performance.

5.2. Inverse hysteresis compensator

The inverse hysteresis model for compensating hysteresis is given by Eq. (21). The density function is chosen as $d_{inv}(\gamma') = \lambda' e^{-\delta' \gamma'}$, and the threshold $\gamma' = \rho' j$ for $j = 1, 2, \dots, 8$. The parameters $g'_0, g'_1, \lambda', \delta'$, and ρ' are determined using the measured input-output data from the forward hysteresis model. The process follows the same steps used to calculate the parameters for the (forward) P-I hysteresis model, where a nonlinear least-square optimization program is applied to determine the parameters as $g'_0 = 1.4583$, $g'_1 = -0.0181$, $\lambda' = 1.4505$, $\delta' = 2.5001$, and $\rho' = 0.1611$.

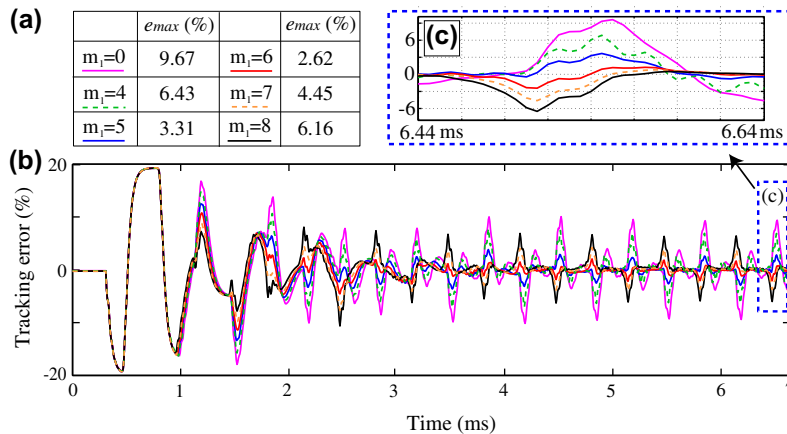


Fig. 12. RC design: determining phase-lead compensator parameter m_1 . (a) $e_{max}(\%)$ versus m_1 . (b) The tracking error of the repetitive controller C_1 with different values of m_1 for the phase lead compensator $P_1(z) = z^{m_1}$. (c) The details of the steady-state tracking error in (b).

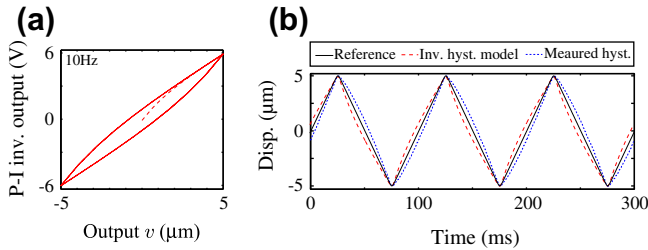


Fig. 13. (a) The inverse hysteresis curve. (b) The inverse hysteresis model (dash line) compared to the measured hysteresis response (dash-dot line) and desired response (solid line).

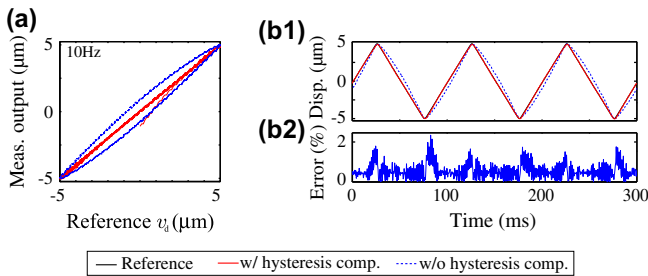


Fig. 14. The performance of the inverse hysteresis compensator (scanning at 10 Hz). (a) The hysteresis curves for the piezoactuator with (solid line) and without (dash line) feedforward hysteresis compensation. (b1) The comparison between the reference and the measured (with hysteresis compensation) output. (b2) The measured tracking error.

The inverse-hysteresis curve is shown in Fig. 13a and its time-response is compared to the measured hysteresis response in Fig. 13b. The \mathcal{H}^{-1} model is applied to compensate for hysteresis in the x -axis actuator of the experimental system at different frequencies to investigate its effectiveness. Fig. 14a and b shows the performance of \mathcal{H}^{-1} for tracking a desired triangle trajectory at 10 Hz. The \mathcal{H}^{-1} compensates for the hysteresis effect, and subsequently linearizes the system and makes the system's output track the reference trajectory, where the maximum tracking error is 2.1% at 10 Hz. The performance of \mathcal{H}^{-1} is further compared to the output response of the dynamic model $G(z)$ in simulation for tracking triangle trajectories at 100 Hz and 1 kHz, since, by compensating for the hysteresis, the output response is dominated by the dynamics effect of $G(z)$. Fig. 15 shows the measured and simulated output versus input plots, where the maximum error is less than 0.92% at 1 kHz. The results show that the hysteresis effect can be effectively compensated for using the proposed inverse model.

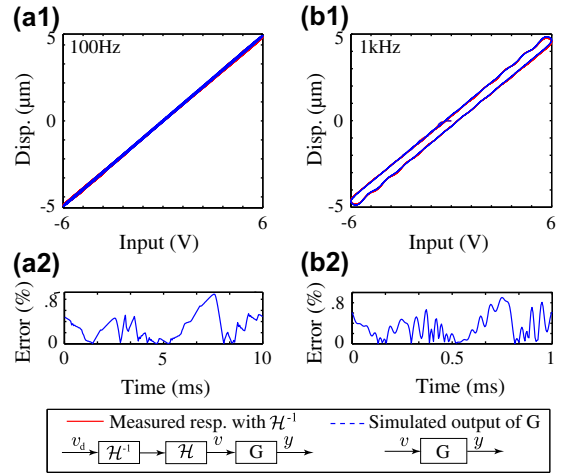


Fig. 15. The comparison between the measured output with hysteresis compensation and the simulated output. (a1) and (a2) 100 Hz triangular trajectory. (b1) and (b2) 1 kHz triangle trajectory.

5.3. Tracking results and discussion

Experiments are performed on the x -axis piezoactuator of the high-speed scanner to verify the effectiveness of the dual-RC on improving the tracking performance compared to traditional PID and conventional RC for tracking triangle trajectories at 1 kHz, 1.5 kHz, and 2 kHz over a 10 μm displacement range. An example tracking result at 1 kHz is presented in Fig. 16. The result compares the tracking performance of the dual-RC to PID control and the conventional RC. Fig. 16b shows the tracking error for each controller and Fig. 16c shows a snapshot of the steady-state tracking performance. The tracking errors are summarized in Table 1, particularly the table shows the maximum tracking error (e_{max}) and the root-mean-square tracking error (e_{rms}). The root-mean-square error is given by:

$$e_{rms}(\%) = \frac{\sqrt{\frac{1}{T} \int_0^T (|y(t)| - |r(t)|)^2 dt}}{\max(r(t)) - \min(r(t))} \times 100\%$$

where T is the signal period time. It is readily seen that the dual-RC provides better performance compared to the conventional RC. In fact, the improvement in tracking precision compared to traditionally-used PID control is over 85%, and to conventional RC is over 48% at 1 kHz, underscoring the benefits of the dual-RC structure.

It is pointed out that if the PID controller is designed around the linear dynamics model (with $K_p = 1.3$, $K_i = 0.5$, and $K_d = 4$),

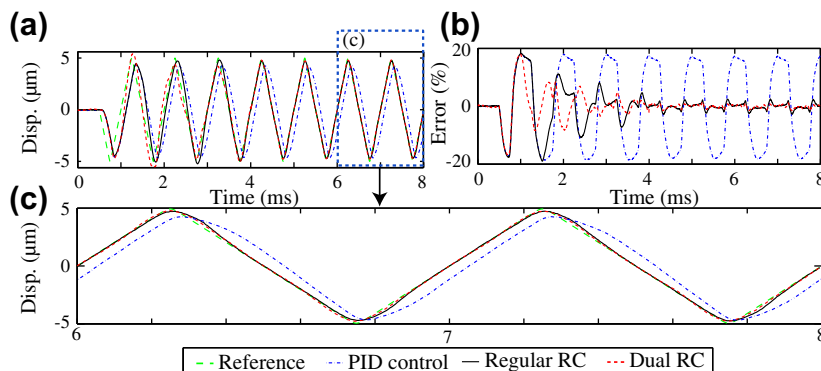


Fig. 16. Experimental results for tracking 1 kHz triangle trajectory for 10 μm displacement. (a) The tracking results. (b) The tracking errors. (c) The detail of the last two periods of the tracking results.

Table 1
Experimental steady-state tracking error for different controllers.

Controller	e_{max} (%)			e_{rms} (%)		
	1 kHz	1.5 kHz	2 kHz	1 kHz	1.5 kHz	2 kHz
PID	17.54	22.46	29.40	14.73	18.87	24.71
PID + conventional RC	4.02	4.36	7.23	1.39	2.07	4.19
PID + dual – RC	2.07	2.91	4.70	0.94	1.07	2.37

simulation shows that the closed-loop system is stable (Fig. 17a). On the other hand, the experimental implementation of the same controller may differ due to the effects of hysteresis. The performance of the \mathcal{H}^{-1} on reducing the effect of hysteresis to improve closed-loop performances is investigated in simulation. Simulation results are provided due to the limited memory space in the FPGA hardware for implementing the combined PID, RC, and \mathcal{H}^{-1} compensator. Particularly, the size of the VHDL codes for the dual-RC combined with \mathcal{H}^{-1} is larger than the allowable memory space of

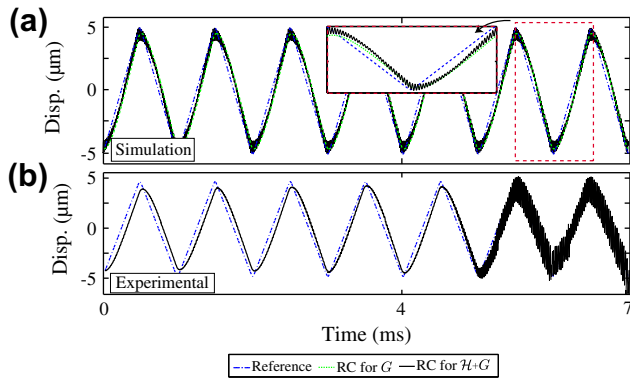


Fig. 17. The effect of hysteresis on closed-loop system stability for tracking 1 kHz triangle trajectory: (a) simulation and (b) experimental.

Table 2
Steady-state tracking error for different controllers.

Controller	e_{max} (%)			e_{rms} (%)		
	1 kHz	1.5 kHz	2 kHz	1 kHz	1.5 kHz	2 kHz
PID + \mathcal{H}^{-1}	11.38	17.02	22.93	10.21	17.61	25.80
PID + conv. RC + \mathcal{H}^{-1}	2.04	2.57	5.73	0.58	1.22	3.69
PID + dual – RC + \mathcal{H}^{-1}	1.08	1.75	2.63	0.42	0.69	1.84

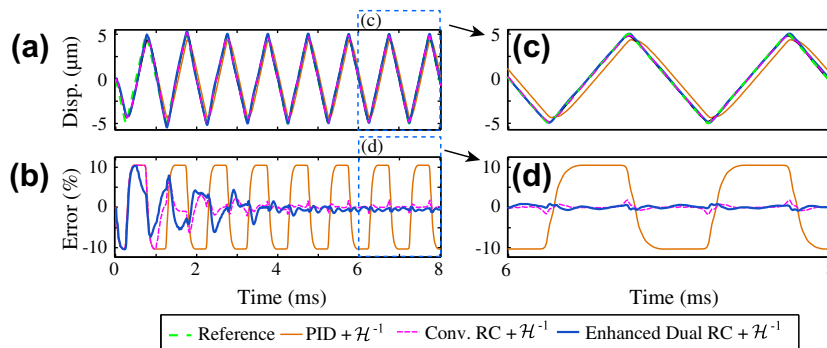


Fig. 18. The simulation results for tracking triangle trajectory at 1 kHz: (a) the tracking results of controllers with \mathcal{H}^{-1} ; (b) the tracking error; (c) and (d) the close-up views of the steady-state stage of tracking results and tracking error respectively.

the FPGA hardware. However, it is pointed out that for low-speed operation, the Matlab xPC Target environment can be used to implement the full control system. For faster operation, FPGA hardware with more memory space can be used.

The simulation results for the regular PID, conventional RC, and dual-RC with \mathcal{H}^{-1} for tracking triangle trajectories at 1 kHz, 1.5 kHz, and 2 kHz are summarized in Table 2. Fig. 18 shows the performance of the dual-RC, conventional RC, and the PID controller with the \mathcal{H}^{-1} at 1 kHz tracking. From the table it can be seen that this process linearizes the plant and the dual-RC enhances the performance of the conventional RC. Hence, the \mathcal{H}^{-1} can reduce the effect of hysteresis on the stability of the RC systems designed around the linear dynamics.

6. Conclusions

Motion control of piezo-based nanopositioning systems is limited by the effects of dynamics and hysteresis. A dual-stage repetitive controller was combined with an inverse hysteresis compensator to address tracking errors due to dynamic and hysteresis effects. Specifically, a dual-stage RC was employed which consisted of a signal generator designed to provide high gains at the fundamental and the harmonics of the reference trajectory and another that offered high gain only at the odd harmonics. An inverse hysteresis compensator was developed based on the structure of the Prandtl–Ishlinskii hysteresis model to linearize the system to enhance the performance of the dual-RC. An analysis was presented for the stability of the dual-RC closed-loop system and the details of the inverse P-I model were discussed. Finally, simulation and experimental results were provided to illustrate the performance improvement of the proposed control scheme compared to conventional RC and industry-standard PID control. The tracking results showed that the inverse hysteresis compensator reduced the hysteresis effect and helped to stabilize the repetitive controlled system. It was also shown that the dual-RC structure reduced the maximum steady-state error compared to conventional RC by approximately 48% (at 1 kHz) and 33% (at 2 kHz). These results demonstrate the benefits of the dual-RC structure and the inverse hysteresis compensator for piezo-based positioning systems.

References

- [1] Radmacher M. Measuring the elastic properties of biological samples with the AFM. IEEE Eng Med Biol 1997;16:47–57.
- [2] Salapaka SM, Salapaka MV. Scanning probe microscopy. IEEE Cont Syst Mag 2008;28(2):65–83.
- [3] Ando T, Uchihashi T, Fukuma T. High-speed atomic force microscopy for nano-visualization of dynamic biomolecular processes. Prog Surface Sci 2008;83(7–9):337–437.

- [4] Francis BA, Wonham WM. The internal model principle of control theory. *Automatica* 1976;12(5):457–65.
- [5] Inoue T, Nakano M, Iwai S. High accuracy control of a proton synchrotron magnet power supply. In: *Proc 8th world congr IFAC*, vol. 20; 1981. p. 216–21.
- [6] Hara S, Yamamoto Y, Omata T, Nakano M. Repetitive control system: a new type servo system for periodic exogenous signals. *IEEE Trans Autom Cont* 1988;33(7):659–68.
- [7] Aridogan U, Shan Y, Leang KK. Design and analysis of discrete-time repetitive control for scanning probe microscopes. *ASME J Dyn Syst Meas Cont* 2009;131:061103 [Special issue on dynamic modeling, control, and manipulation at the nanoscale, 12 pages].
- [8] Chew KK, Tomizuka M. Digital control of repetitive errors in disk drive systems. *IEEE Cont Syst Mag* 1990;10(1):16–20.
- [9] Steinbuch M, Weiland S, Singh T. Design of noise and period-time robust high-order repetitive control, with application to optical storage. *Automatica* 2007;43(12):2086–95.
- [10] Li CJ, Li SY. To improve workpiece roundness in precision diamond turning by in situ measurement and repetitive control. *Mechatronics* 1996;6(5):523–35.
- [11] Chen S-L, Hsieh T-H. Repetitive control design and implementation for linear motor machine tool. *Int J Mach Tools Manuf* 2007;47(12–13):1807–16.
- [12] Arimoto S, Kawamura S, Miyazaki F. Bettering operation of robots by learning. *J Robotic Syst* 1984;1(2):123–40.
- [13] Moore KL, Dahleh M, Bhattacharyya SP. Iterative learning control: a survey and new results. *J Robotic Syst* 1992;9(5):563–94.
- [14] Leang KK, Devasia S. Design of hysteresis-compensating iterative learning control for piezo positioners: application to atomic force microscopes. *Mechatronics* 2006;16(3–4):141–58.
- [15] Wu Y, Zou Q. Iterative control approach to compensate for both the hysteresis and the dynamics effects of piezo actuators. *IEEE Cont Syst Technol* 2007;15(5):936–44.
- [16] Clayton GM, Tien S, Leang KK, Zou Q, Devasia S. A review of feedforward control approaches in nanopositioning for high speed SPM. *ASME J Dyn Syst Meas Cont* 2009;131(6):061101 [Special issue on dynamic modeling, control, and manipulation at the nanoscale, 19 pages].
- [17] Croft D, Shed G, Devasia S. Creep, hysteresis, and vibration compensation for piezoactuators: atomic force microscopy application. *ASME J Dyn Syst Meas Cont* 2001;123(1):35–43.
- [18] Lowrie F, Cain M, Stewart M, Gee M. Time dependent behaviour of piezoelectric materials. Technical report 151. National Physical Laboratory; 1999.
- [19] Lee H-J, Saravanos DA. The effect of temperature dependent material properties on the response of piezoelectric composite materials. *J Intell Mater Syst Struct* 1998;9(7):503–8.
- [20] Fantner GE, Hegarty P, Kindt JH, Schitter G, Cidade GAG, Hansma PK. Data acquisition system for high speed atomic force microscopy. *Rev Sci Instr* 2005;76(2):026118-1–8-4.
- [21] Tomizuka M, Tsao TC, Chew KK. Discrete time domain analysis and synthesis of repetitive controllers. In: *American control conference*; 1988. p. 860–6.
- [22] Ratcliffe JD, Lewin PL, Rogers E. Stable repetitive control by frequency aliasing. *Intell Cont Syst Optim* 2005:323–6.
- [23] Broberg HL, Molyet RG. A new approach to phase cancellation in repetitive control. In: *IEEE Industry Applications Society annual meetins*, vol. 3; 1994. p. 1766–70.
- [24] Zhou K, Wang D, Zhang B, Wang Y, Ferreira JA, de Haan SWH. Dual-mode structure digital repetitive control. *Automatica* 2007;43:546–54.
- [25] Zhou K, Wang D, Zhang B, Wang Y. Plug-in dual-mode-structure repetitive controller for CVCF PWM inverters. *IEEE Trans Ind Electron* 2004;56(3):784–91.
- [26] Kim B-S, Tsao T-C. A performance enhancement scheme for robust repetitive control system. *ASME J Dyn Syst Meas Cont* 2004;126(1):224–9.
- [27] Main JA, Garcia E. Piezoelectric stack actuators and control system design: strategies and pitfalls. *AIAA J Guid Cont Dyn* 1997;20(3):479–85.
- [28] Shan Y, Leang KK. Repetitive control with Prandtl–Ishlinskii hysteresis inverse for piezo-based nanopositioning. In: *American control conference*, invited session on advances in control of nanopositioning and SPM systems, St. Louis, MO; 2009. p. 301–6.
- [29] Brokate M, Sprekels J. *Hysteresis and phase transitions*. New York: Springer; 1996.
- [30] Kuhnen K. Modeling, identification and compensation of complex hysteretic nonlinearities: a modified Prandtl–Ishlinskii approach. *Eur J Contr* 2003;9(4):407–18.
- [31] Janaideh MA, Su C-Y, Rakheja S. Development of the rate-dependent Prandtl–Ishlinskii model for smart actuators. *Smart Mater Struct* 2008;17:035026. 11pp.
- [32] Kim JD, Nam SR. A piezoelectrically driven micro-positioning system for the ductile-mode grinding of brittle materials. *J Mater Process Technol* 1999;61(3):309–19.
- [33] Chen BM, Lee TH, Hang CC, Guo Y, Weerasorriya S. An H_∞ almost disturbance decoupling robust controller design for a piezoceramic bimorph actuator with hysteresis. *IEEE Trans Control Syst Technol* 1999;7(2):160–74.
- [34] Song J, Armen DK. Generalized Bouc–Wen model for highly asymmetric hysteresis. *J Eng Mech* 2006;132(6):610–8.
- [35] Adriaens HJMTA, de Koning WL, Banning R. Modeling piezoelectric actuators. *IEEE/ASME Trans Mech* 2000;5(4):331–41.
- [36] Banning R, de Koning WL, Adriaens HJMTA, Koops RK. State-space analysis and identification for a class of hysteretic systems. *Automatica* 2001;37:1883–92.
- [37] Michael G, Nikola C. Modeling piezoelectric stack actuators for control of micromanipulation. *IEEE Cont Syst Mag* 1997;17(3):69–79.
- [38] Ge P, Jouaneh M. Tracking control of a piezoceramic actuator. *IEEE Trans Cont Syst Technol* 1996;4(3):209–16.
- [39] Ge P, Jouaneh M. Generalized Preisach model for hysteresis nonlinearity of piezoceramic actuators. *Precision Eng* 1997;20:99–111.
- [40] Yu Y, Xiao Z, Naganathan NG, Dukkupati RV. Dynamic Preisach modelling of hysteresis for the piezoceramic actuator system. *Mech Mach Theory* 2002;37:75–89.
- [41] Ahn H-S. Design of a repetitive control system for a piezoelectric actuator based on the inverse hysteresis model. In: *The fourth international conference on control and automation*, Montreal, Canada; 2003. p. 128–32.
- [42] Fleming AJ, Moheimani SOR. A grounded-load charge amplifier for reducing hysteresis in piezoelectric tube scanners. *Rev Sci Instr* 2005;76:073707-1.
- [43] Leang KK, Zou Q, Devasia S. Feedforward control of piezoactuators in atomic force microscope systems: inversion-based compensation for dynamics and hysteresis. *IEEE Cont Syst Mag* 2009;29(1):70–82 [Special issue on hysteresis].
- [44] Costa-Castello R, Grino R, Fossas E. Odd-harmonic digital repetitive control of a single-phase current active filter. *IEEE Trans Power Electron* 2004;19(4):1060–8.
- [45] Zhou K, Doyle JC. *Essentials of robust control*. Prentice-Hall, Inc.; 1998.
- [46] Fleming AJ, Leang KK. Charge drives for scanning probe microscope positioning stages. *Ultramicroscopy* 2008;108:1551–7.
- [47] Leang KK, Fleming AJ. High-speed serial-kinematic AFM scanner: design and drive considerations. *Asian J Cont* 2009;11(2):144–53 [Special issue on advanced control methods for scanning probe microscopy research and techniques].
- [48] Kenton BJ, Fleming AJ, Leang KK. A compact ultra-fast vertical nanopositioner for improving scanning probe microscope scan speed. *Rev Sci Instr* 2011;82:123703.
- [49] Kenton BJ, Leang KK. Design, characterization, and control of a monolithic three-axis high-bandwidth nanopositioning stage. In: *American control conference*; 2010. p. 4949–56.